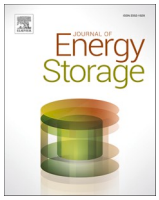
Journal of Energy Storage 94 (2024) 112371



Contents lists available at ScienceDirect

Journal of Energy Storage

journal homepage: www.elsevier.com/locate/est



Research papers



Validation of Sahraei Failure Criterion on cylindrical and pouch Lithium-ion battery cells

Yihan Song [a], Marian Bulla [b], Huzefa Patanwala [a], Elham Sahraei [a,*]

[a] Electric Vehicle Safety Lab (EVSL), Department of Mechanical Engineering, Temple University, 1947 N 12th St, Room 929, Philadelphia, PA 19122, USA
[b] Altair Engineering GmbH, Josef-Lammerting-Allee 10, 50933 Cologne, Germany

ARTICLE INFO

Keywords:
Li-ion battery saftey
Finite element method
Failure model for jellyroll
Pouch cell/cylindrical cell
Short circuit criterion
Sahraei failure criterion

ABSTRACT

Safety is a major concern for Li-ion batteries in Electric Vehicles (EVs). Internal fracture of a battery cell may lead to a short circuit, and in extreme cases, cause thermal runaway and explosion. Consequently, heavy protective structures are used around EV battery packs to ensure zero deformation in the event of a vehicle crash. Having a universal failure model for battery short circuits can enable better prediction of imminent safety concerns and provide a tool for designing optimized protective structures. In this work, a failure and short circuit model titled the "Sahraei Failure Criterion" derived from simulations of the microstructure of the electrode-separator assembly, is developed and employed to predict cell failures for two types of cylindrical cells and one pouch cell. The failure model, in combination with a homogenized cell model, is validated in predicting all major loading scenarios, including local hemispherical and rod indentations, three-point bending and in-plane loading. This failure model defines the jellyroll's in-plane failure strain values as a function of the ratio of through-thickness compressive strain to in-plane tensile strain. A user-defined FORTRAN code has been used to implement the Sahraei failure criterion in RADIOSS. This universal failure model predicts the onset of internal fracture of the jellyroll under all available types of loadings with a single calibrated input curve. The model is also now programmed in the commercial software Altair RADIOSS (and OpenRadioss) as /FAIL/SAHRAEI criteria and is currently being implemented in Ansys LS-DYNA under the *MAT_MODIFIED_HONEYCOMB keyword to be available for users of both software.

1. Introduction

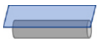
Tremendous increase of EVs on the road has created a huge demand for Li-ion batteries all over the world [1]. Two of the most popular batteries form factors on the market are cylindrical and pouch battery cells, which are used by thousands to make battery packs of many vehicles on the road today [2].Compared with traditional vehicles with internal combustion engines, EVs' power come from the battery pack. Since batteries are sensitive to the working environments and a potential deformation, maintaining safety dictates the design of the enclosure and structure of the protective package [3]. External loading that improvises the exterior cover can cause deformation to battery cells which may lead to failure of the electrodes and separator and ultimately cause short circuit, thermal runaway, and explosion [4,5]. This highlights the need for having a proper model to get accurate prediction on deformation and internal failure of the battery.

In 2012, the first set of mechanical tests on full cylindrical and pouch lithium-ion cells, with first homogenized models to predict their deformation and failure, were published by Sahraei et al [6,7]. Over the past ten years, several other models had been proposed with different materials and failure models for the jellyroll/electrode stack and shell casing of the cell [8–19].For cylindrical study, the metal shell casing as the stiff protection of the cell has been tested and modeled in order to get proper full cell model [20,21]. Except for cylindrical and pouch cell, failure of prismatic cell under mechanical abuse has also been studied for safety improvement purpose [22–24]. Besides quasi-static loading experiments, dynamic loading is also a hot topic since it is similar to crashworthiness problems. Raffler published the research about Li-ion pouch cell mechanical response under high strain rate and different impact orientations [25]; prismatic cell and cylindrical cell testing and modeling under dynamic loadings are also developed [26,27]. Additionally, there are several studies focused on testing and modeling deformation and failure of single components of a battery cell like electrodes and separators [28–32]. Other researchers have extended

* Corresponding author.
E-mail address: elham.sahraei@temple.edu (E. Sahraei).

https://doi.org/10.1016/j.est.2024.112371
Received 15 January 2024; Received in revised form 18 April 2024; Accepted 29 May 2024
Available online 8 June 2024
2352-152X/© 2024 The Authors. Published by Elsevier Ltd. This is an open access article under the CC BY-NC-ND license (http://creativecommons.org/licenses/by-nc-nd/4.0/).

Table 1
Contribution comparison with previous works.

Cylindrical/ Elliptical cell									
	Model type	Homogenized (H) Detailed (D)	Failure criteria for jellyroll	Validation of Failure Criteria with One Set of Parameters V: validated, RC: recalibrated, and N: no validation simulation					
									
Sahraei 2012 [6]	Full cell	H	Tensile stress cut off value	V	V	N	N	N	
Greve 2012 [9]	Quarter cell	H	Stress-based (Universal)	N	N	N	N	N	
Wierzbicki & Sahraei 2013 [14]	Full cell	H	Tensile stress cut off value	V	V	N	N	N	
Sahraei 2015 [55]	Full cell	H	Maximum tensile strain at failure	RC	RC	N	N	N	
Xu 2015 [59]	Full cell	H	Double shear stress-based (Universal)	N	N	N	N	N	
Sahraei 2016 [57]	Full cell	H	Maximum tensile strain at failure	N	V	RC	N	N	
Sheikh 2018 [19]	Full cell	D	Maximum tensile strain at failure (Component)	RC	N	RC	RC	N	
Wang & Xu 2019 [52]	Full cell	D	Triaxiality-based (Component)	V	N	V	V	V	
Gilaki 2021 [60]	Full cell	H	Maximum tensile strain at failure	RC	RC	RC	RC	N	
Song 2022 [50]	Full cell	H	Maximum tensile strain at failure	RC	RC	RC	RC	RC	
This work	Full cell	H	Sahraei failure (Universal)	V	V	V	V	V	

Pouch cell									
	Model type	Homogenized(H)/ Detailed(D)	Failure criteria for jellyroll	Validation of Failure Criteria with One Set of Parameters V: validated, RC: recalibrated, and N: no validation simulation					
									
Sahraei 2014 [61]	Full cell	H	Maximum principal strain (simple)	V	V	N	N	N	N
Zhang 2015 [62]	Quart Cell	D	Separator Strain-based	V	V	N	N	N	N
Zhang & Xu 2017 [32]	Full cell	H	Strain-based with damage	N	N	N	N	N	N
Chung 2018 [10]	Full cell	H	Stress-based	RC	RC	N	RC	N	N
Keshavarzi 2022 [18]	Full cell	H	Maximum tensile strain at failure	RC	RC	RC	RC	RC	RC
This work	Full cell	H	Sahraei failure (universal)	V	V	V	V	V	V

components and cell level models into evaluation of the response at the battery pack level [28,33–36].Isotropy and anisotropy for component level testing and cell level FEM modeling was also been studied [37,38]. Relation between failure strain and state of charge has been discussed by Xu et al., 2016 [39]. The most insight into the fracture mechanism of the jellyroll/electrode stack comes from studies of deformation at the micro structural level, which is the basis of the research presented in these works [40–44].With the increase of the demand of Li-ion battery life-time research, the relation between compressive loadings and cell life-time has also been studied by Barai et al [45].

Here, we will first review the most common failure models discussed and used in the literature in general, and then focus on the ones that have been applied to the jellyroll/electrode stack of lithium-ion batteries. One typical type of failure model is the simple single parameter one, where defining a single indicator for failure, like strain or stress value is identified as the criterion. For body-centered cubic (BCC) materials, maximum principal stress is commonly used as indicator of the brittle fracture predictions [46,47]. Maximum shear stress is one of the oldest failure criteria used for rock or soil [48]. Maximum principal strain failure model has also been very popular for battery simulations. From the first use by Sahraei et al. [49], lots of studies had been using the principal strain as the failure indicator [6,14,50]. For this model, the failure strain is calibrated from through-thickness loading experiments. This model then predicts failure accurately for dominantly through-thickness compressive loads, such as local indentations with a hemispherical/flat punch or rod indentation. The problem with this single parameter failure model is that it cannot have a good prediction in cases with major tensile loading or when loads are not in through-thickness direction, such as three-point bending and in-plane loading. Another very common type of failure model is the one which defines failure strain or stress as a function. Typical examples are Johnson-Cook (JC), Cockcroft-Latham (CL) and modified Mohr-Coulomb (MMC) models. These models define failure strain as a function of triaxiality or both triaxiality and lode angle parameter. It has been proven that the failure strain for metals is different under compression and tension. For battery models, failure of shell casing, as the major load bearing metal component of the cylindrical and prismatic cells, had been predicted accurately with such models [21,24,50,51], where the cell has been modeled with two major components, a homogenized jellyroll and a metal casing. Wang et al. 2019 also used this method to account for the failure of shell casing in their detailed models [52]. Those failure criteria can also be used for the jellyroll metal components, such as metal current collectors and separator [50,53–55]. However, this kind of criteria has not been reported to be successful in prediction of failure for a homogenized model of the jellyroll/electrode stack. Since the electrode stack/ jellyroll is comprised of several layers of porous polymeric/ granular materials in addition to the metallic ones, a universal failure model, considering the complexities of all layers and the interactions between them in various types of loadings, must be identified to make accurate predictions for a homogenized material representing all layers.

Table 1 shows the previous battery cell models with failure criteria coupled. Many studies predicted the jellyroll failure with single parameter criteria. The most popular one is maximum principal failure strain criterion. For this model, a single failure strain value is calibrated,

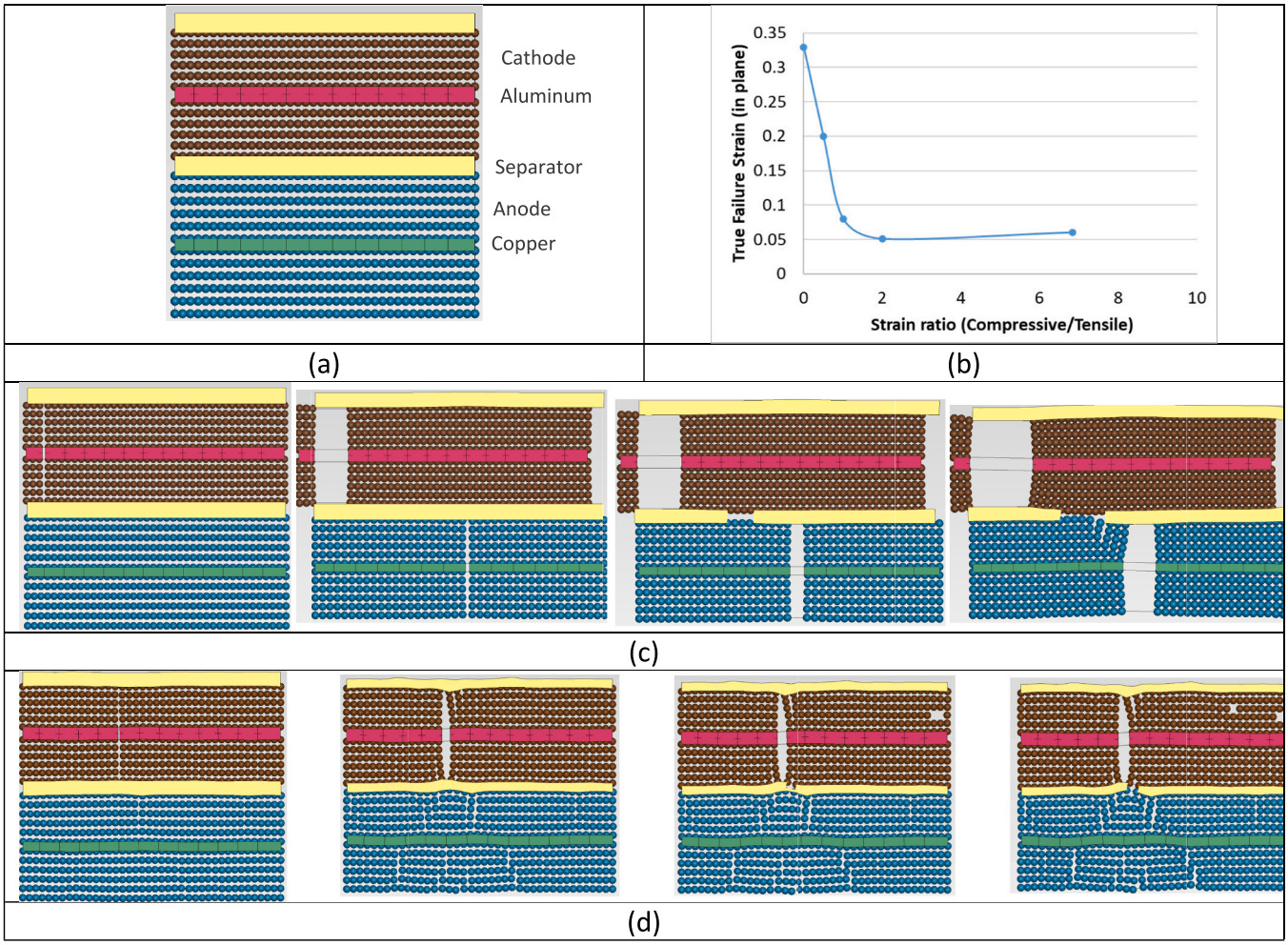


Fig. 1. Sahraei 2016 model failure strain versus ratio of compressive to tensile strain (strain ratio): (a) Undeformed RVE model. (b)Curve of failure strain vs strain ratio. (c) RVE failure with tension dominated. (d) RVE failure with compression dominated.

usually from simulation of a hemispherical punch loading case, using the location of force drop, which coincides with location of voltage drop for the cases with voltage measurements, as the exact position of element erosion. Such failure models have been validated with a few loading cases, including the ones with major through-thickness compression loading. However, when the loading becomes more complex, the failure will not be predicted correctly with this single value model. In some past studies, to track the changes in failure strain for different load cases, the failure strain was recalibrated. However, this cannot be considered a universal failure model when new calibration is needed for a new load case. The past work of some of the current authors mostly fall under this category [18,50,54,55]. In an attempt to find alternative failure models, Chung et al. proposed using stress-based Mohr Columb criteria and validated that again for dominantly through-thickness compression cases of hemispherical and punch indentations [10]. Greve et al. and Zhang & Xu et al. proposed their own failure criteria based on modeling various loading cases and monitoring the stress conditions, but the proposed models lack implementation and validation [9,56]. In 2016, Sahraei et al. used a model of a Representative Volume Element (RVE) of a cell and demonstrated a failure locus based on simulations of the deformation and failure of layers of the electrode-separator assembly under various complex loading scenarios. They verified this model for two load cases. However, that model had not been implemented in software and remained unvalidated to this date [57].

A summary of the above studies has been presented in Table 1. One may see under validation section three different notations, V: meaning validated, RC: meaning recalibrated for prediction of different load cases, which in essence means no universal validation, and N: meaning no validation simulation was performed. It can be observed that to the author's knowledge, no published failure model for battery jellyrolls before the present work has been validated in all the loading scenarios without recalibration of the failure parameters in different loading cases.

For the current work, an extension of the 2016 Sahraei [57] et al. has been completed, further investigating failure mechanisms using an RVE approach. Then the model was implemented in Altair RADIOSS software as well as in OpenRadioss [58] and calibrated for two commercial cylindrical cells and one pouch cell. The main contribution of the current work is to develop and calibrate a universal failure model for jellyroll/electrode stack that can predict failure (or lack of it) accurately for all loading cases in the literature, including local indentation, bending and in-plane loading, with one set of calibration parameters.

2. Method

2.1. RVE based on the Sahraei failure model

In 2016, Sahraei et al. used computational homogenization to simulate deformation and failure of a RVE for an elliptical cell. This method is a numerical technology used to simulate the homogenous behavior of multi-materials structures by considering the properties of microstructure [63–66]. The interior of battery cells is made of different

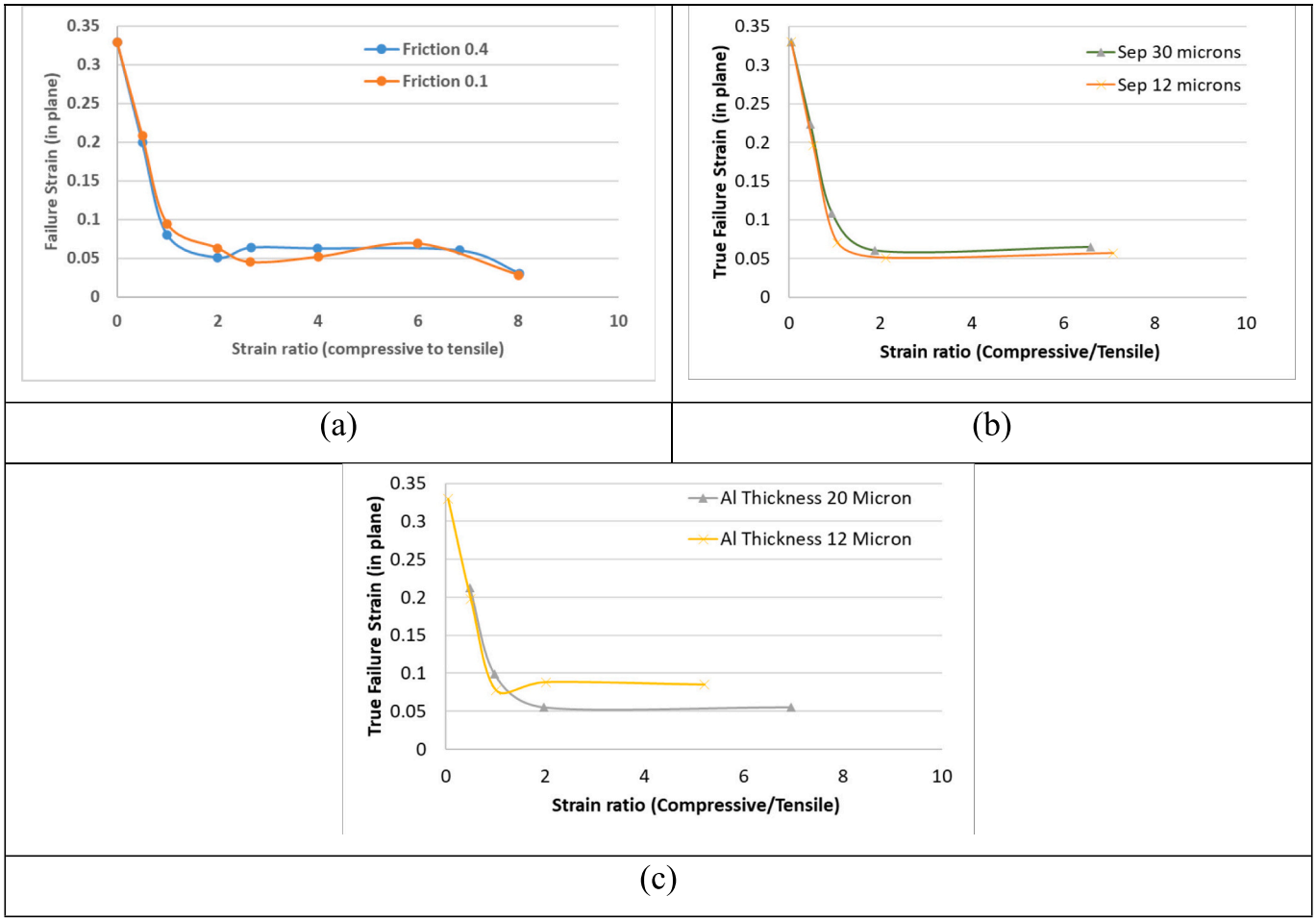


Fig. 2. Sequence of loading and failure in pure compression, in-plane tension, and combined loading of the RVE [57]: (a) Different simulations with 0.1/0.4 friction. (b) Different simulations with 12/30 μm separator thickness. (c) Different simulations with 12/20 μm Al current collector thickness.

material layers including anodes, cathodes, metal current collectors and separators. The RVE is the smallest unit that repeats in the cell and can make the whole cell. Homogenization provides the possibility to obtain the jellyroll behavior in macro-scale based on the response of the various interior components in micro scale. In the absence of body forces, the mechanical equilibrium for micro- and macroscale can be written as:

$$\nabla P_m = 0, \text{in V, RVE volume.} \quad (1)$$

$$\nabla P_M = 0, \text{in } V_0, \text{Domain volume.} \quad (2)$$

Here, P_m is the first Piola-Kirchhoff stress tensor in microscale; P_M is the first Piola-Kirchhoff stress tensor in macroscale. The relation between micro- and macroscale stress tensor can be written as [34,57]:

$$P_M = \frac{1}{V_0}\int_{V_0} P_m dV_0 \quad (3)$$

Sahraei et al [57] developed a micro-scale RVE for the battery cell by modeling each component of the electrode-separator assembly individually, see Fig. 1a: separator (yellow color), copper and aluminum (red/green color), coating of the electrodes (blue/brown color). The porous anode and cathode coatings were modeled with crushable foams, while the metal current collectors were defined by piecewise linear plasticity models. The separator was modeled with a combination of crushable foam behavior under compression and a plasticity model under tension. Each layer was assigned its material and failure properties based on its own response observed in single layer tensile/compressive and biaxial testing [57]. The thickness of the separator was 20 μm and its failure criterion was a principal tensile failure of 0.33 mm/mm. The aluminum foil layer was 16 μm and was assigned a failure value of 0.049 equivalent plastic strain. The copper layer was 9 μm thick and was assigned a 0.178 equivalent plastic strain. For the details of the material data for each layer of the model, readers are advised to review the reference paper by Sahraei et al. [57] The RVE consisting of the layers of electrode-separator assembly was then used to simulate deformation and failure under a combination of through thickness compression/tension and in-plane tension loads. A failure locus was plotted based on simulation of five different cases of through thickness-in plane strain ratios, ranging from pure in-plane tension with no through thickness compression to pure through thickness compression with no applied in-plane tension, See Fig. 1b. Kermani et al. later added simulation of in-plane compressive loads with a similar but longer RVE [67]. These studies showed that under pure in-plane tension, there is no interaction between different layers of the RVE, therefore, short circuit is due to failure of the separator at a strain value equal to that of the separator itself, which is 0.33 mm/mm, see Fig. 1b. When compression between the layers increases, the interaction between the layers increases as well. Therefore, the early failure of current collectors will localize the deformation of separator and leads to an early failure of separator, causing short circuit at tensile strain values of about 0.05 mm/mm. Fig. 1c and d show the sequence of failure of layers under combination of tensile and compressive loads, while in Fig. 1c, they are dominantly tensile versus in Fig. 1d they are mostly compressive. In cases of through thickness tension, the layers just separate from each other, and no short circuit will be initiated. Also, in-plane compression ultimately causes buckling of the layers but does not

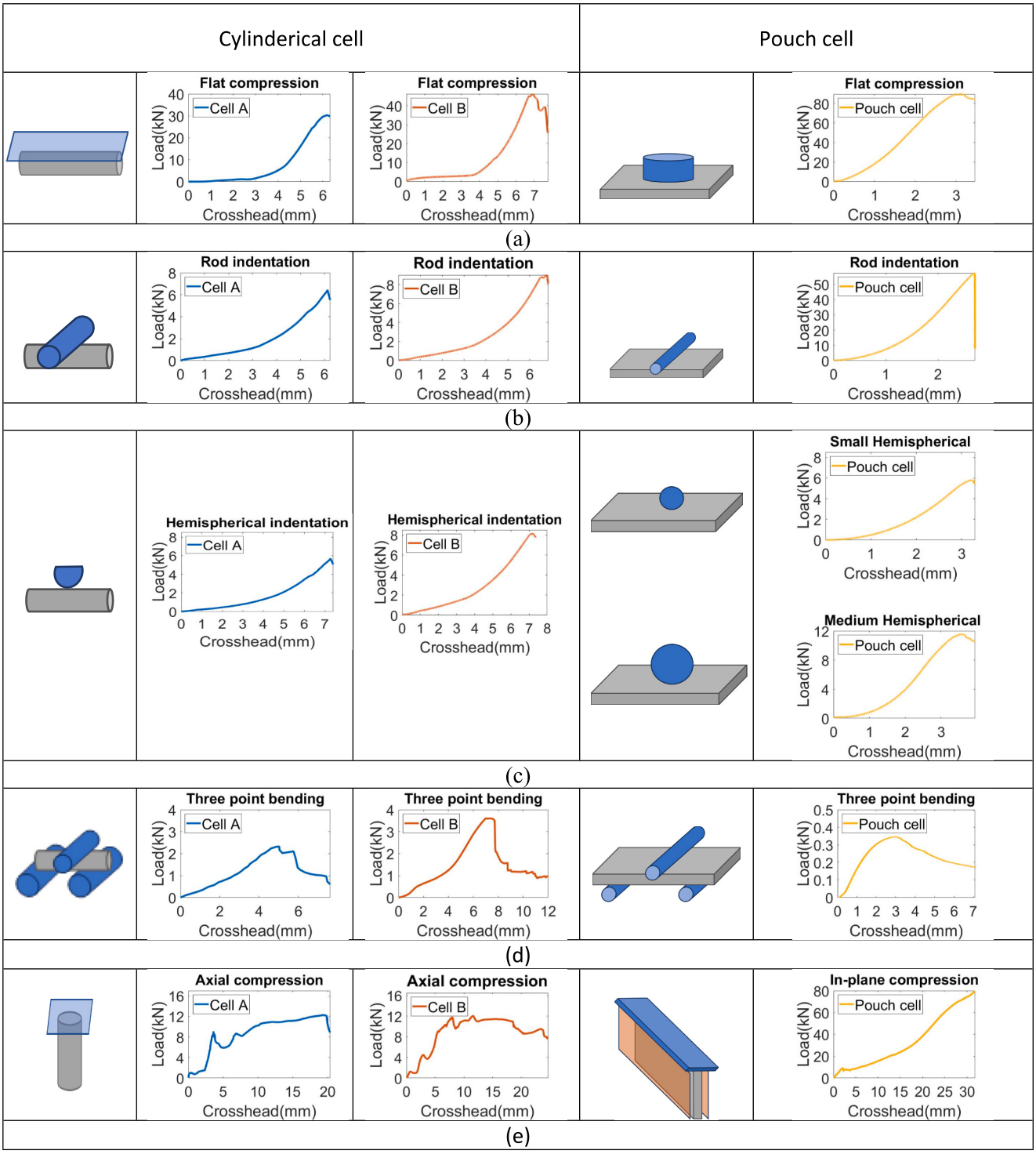


Fig. 3. Experiment schematics and results for cell A: (a) flat compression (b) Rod indentation (c) Hemispherical indentation (d) Three-point bending (e) Axial/In-plane compression.

lead to short-circuit or causing fracture in the layers. Pure shear also just causes sliding of the layers over each other with no failure.

To further understand the failure response of this RVE, additional simulations were performed in this work. In a first attempt, additional strain ratios were simulated to generate a total of eight points for the failure locus to make sure the function will not behave significantly differently in the ranges of strain ratios that were not modeled previously. Then, to understand the effects of friction between the layers, two extreme cases of friction of 0.1 and 0.4 were simulated for all the above cases. Fig. 2a shows the failure locus for all the simulated cases with the two friction values. These simulations showed similar trends with minimal changes for all load cases, hence confirming the stability of this failure locus as a function between the two identified variables. To verify how changes in a separator layer can affect the failure locus, additional simulations were performed for an RVE with a separator thickness of 30 μ and 12 μ. These values were chosen based on the thickness of commercially available separators on the market. To verify the effects of current collector failure, additional simulations were performed with

aluminum current collectors of 12 μ and 20 μ thickness. This variation again was chosen based on commercially available aluminum current collectors on the market. Fig. 2b, and c show the observed changes in the failure locus based on the variations in the layers' properties above. The main purpose of these simulations was to observe the effects of changes in each of the layers on the final shape of the failure locus. It can be observed that a thicker separator may not have any significant effects on the failure locus, as the lower section of the failure locus is limited to the failure of the aluminum current collector. The reduction in thickness of the current collector however reduces the contribution of its strength. Therefore, at the onset of failure of current collector, a smaller pulse is transferred to adjacent layers and the localization of deformation in the separator is delayed. This change raises the lower limit of failure strain for the RVE with a thinner aluminum current collector. The above simulations show that the RVE Based failure locus can connect the response of the microstructure of the cell to its homogenized failure properties. In the next step, one needs to evaluate whether this failure locus can predict the failure in full cell homogenized models.

To continue evaluation of this failure criterion, in the current work, a user defined code was implemented in the commercial software RADIOSS. This code, titled Sahraei failure criterion (/FAIL/SAHRAEI), defines the failure of a homogenized jellyroll using the in-plane tensile strain to failure as a function of the ratio of through thickness compression strain over in-plane tensile strain. Then the model was calibrated for two cylindrical cells, named here cell A and cell B and one pouch cell to verify its capability in predicting failure in various loading cases.

A FORTRAN code is used to define the failure model based on the strain ratio. In the code we define the ε_{11} as the through-thickness direction (x direction in Fig. 4), looking for compressive strain; ε_{22} as the hoop direction which is the machine direction of the separator (y direction in Fig. 4); ε_{33} as the axial direction which is the transverse direction of the separator (z direction in Fig. 4). The ratios are calculated as $c_2 = \frac{\varepsilon_{11}}{\varepsilon_{22}}$ and $c_3 = \frac{\varepsilon_{11}}{\varepsilon_{33}}$. The code will then look for the corresponding failure strain value in each direction of anisotropy (ϵ_{f2} *and* ϵ_{f3}) based on the current strain ratio at each time step. If the plastic strain is greater than the defined failure strain value, the element will then be deleted as an indication of failure.

In summary, the model will be:

$$c_i = \frac{\varepsilon_{11}}{\varepsilon_{ii}} \; i = 2 \text{ and } 3 \tag{4}$$

$$\epsilon_{fi} = f(c_i) \; \text{i} = 2 \text{ and } 3 \tag{5}$$

2.2. Battery specification

Two commercial 18650 cylindrical cells and one commercial pouch cell were used for model calibration and validation. The first cylindrical commercial cell, here referred to as Cell A, had lithium cobalt dioxide chemistry, with 2600mAh capacity and 3.7 V normal voltage [6]; and a second cylindrical commercial cell, here referred to as Cell B, with lithium-iron-phosphate, had 1500mAh nominal capacity and 3.2 V average voltage. A full cylindrical cell model here contained two parts: shell casing and jellyroll. Each part had been previously characterized and associated homogenized models were calibrated to have good prediction of load-displacement and shape of deformation under lateral and axial loadings as well as three-point bending [50,53]. In this paper, the models were updated to use the /FAIL/SAHRAEI failure criteria for fracture of the jellyroll. The full failure locus for each cell was calibrated by using the failure strain and strain ratios for individual loading cases.

The pouch cell used in this study was a commercial cell with NMC chemistry commonly used in manufactured electric vehicles. This pouch cell has a geometry of 11.43*110*310 (Thickness*Width*Length in mm). The nominal capacity and voltage are 60 Ah and 3.68 V. Discharge cut-off voltage for this cell is 3 V. Compared with cylindrical cells, pouch cell doesn't have the metal shell casing, it only uses a very thin polymer pouch to carry the cell, which means the whole cell can be homogenized in one part. The pouch cell model also was similarly coupled with a /FAIL/SAHRAEI criterion which was calibrated to predict the failure in all loading cases.

2.3. Description of experiments for cylindrical and pouch cells

Here we provide a short summary of the experiments available for each of these cells from the previous work of the authors [6,7,53,68,69] as well as new experiments performed for the current study. Five tests were conducted for both cell A and cell B: rod and hemispherical indentation, flat compression, three-point bending and axial compression. Both cylindrical cells were fully discharged before conducting the experiments. Cell A was tested on an MTS load frame with displacement control and a 10 kN load cell, the rate of loading was 1 mm per minute and data was recorded at 1 Hz sampling rate at an accuracy of 1 %. A Radio Shack Digital Multimeter with an accuracy of 0.3 % and same sampling rate was used for voltage measurement [6]. Experiments of cell B and pouch cell were performed on an Instron 5985 load frame with a 250 kN load cell and similar accuracy and sampling rate. An LVDT deflection sensor (model 2601–043) was also used to ensure the accuracy of the displacement measurement [53]. For all tests, displacements were applied at 1 mm/min, except for cell B's three-point bending test, where a 0.25 mm/min rate was used to obtain better observation of the fracture. All tests are performed twice to ensure repeatability. Six tests were conducted for the pouch cell, including 2 different hemispherical indentations, rod indentation, flat compression, three-point bending and in-plane compression test. The test data was highly consistent for all test types, as also reported for this kind of test in previous publications of the authors [69]. Therefore, here we plot one data for every single test to have better visualization, especially for comparison with FEM model validation in Section 4. Batteries were charged and discharged for 5 cycles and were tested with 0 % state-of-charge. Experimental data for all cells are summarized in Fig. 3, a brief explanation of each test scenario is included below.

2.3.1. Flat compression

In the compression tests, a battery cell was laid on a fixed flat plate and compressed by a moving flat plate on the top. Cell A has a peak force of 30 kN at 6 mm displacement; while cell B has a peak force of 45 kN at 6.8 mm displacement, see Fig. 3(a). The cell was packed into a plastic bag for safety protection. For the pouch cell, since the cell has a large geometry, test force will be too high if the full surface of the cell is compressed. Therefore, a flat cylindrical punch has been used for the pouch cell. The diameter of the punch is 40 mm. Pouch cell exhibis a peak force of 90 kN at 3 mm displacement.

2.3.2. Rod indentation

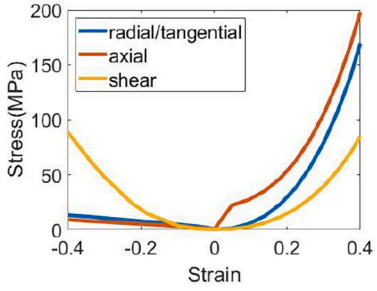
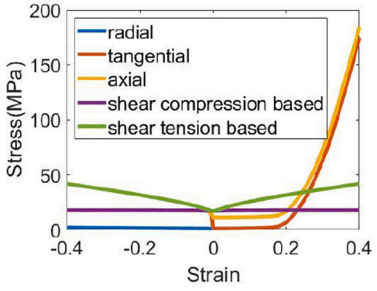
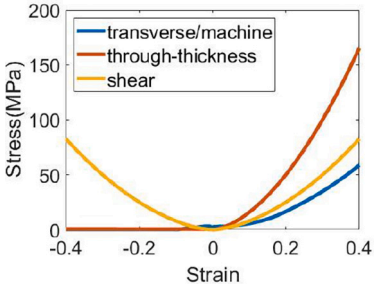
In this test, the cell was placed on a flat plate and indented by a rod indenter. There is a slight difference between cell A and cell B's rod indentation. The rod indenter is 16 mm in diameter. The peak force of cell A is 6.4 kN at displacement 6.3 mm; cell B has a 9 kN peak force at displacement 6.5 mm. The rod indenter for pouch cell also has 16 mm diameter, and the peak force is around 60 kN with 2.7 mm displacement. See Fig. 3 (b) for a summary of all rod indentation tests.

2.3.3. Hemispherical indentation

Both cell A and cell B are using a 12.7 mm hemispherical indenter for this test. For cell A, 5.8 kN peak force was obtained at 7.4 mm displacement; for cell B, 8.1 kN peak force was obtained at 7.2 mm displacement, see Fig. 3 (c).

Two different hemispherical tests were performed for the pouch cell, the small one used a 12.7 mm diameter where the medium test used a 25.4 mm diameter hemispherical indenter. Small hemispherical test had a 5.9 kN peak force at 3.2 mm displacement; the medium one had 11.8

Table 2
Material properties for cylindrical (cell A and B) and pouch cell's jellyroll.

Cell A		
Elastic modulus for three directions of anisotropy 500 MPa Poisson's ratio for bulk material 0.3	Shear modulus for three directions of anisotropy 250 MPa Yield stress for bulk material 200 MPa	Young's Modulus for bulk material 79 GPa
Cell B		
Elastic modulus for three directions of anisotropy 1000 MPa Poisson's ratio for bulk material 0.3	Shear modulus for three directions of anisotropy 500 MPa Yield stress for bulk material 200 MPa	Young's Modulus for bulk material 79 GPa
Pouch cell		
Elastic modulus for transverse direction 2460 MPa Shear modulus for transverse/machine 1230 MPa	Elastic modulus for machine direction 2460 MPa Shear modulus for machine/through-thickness 50 MPa	Elastic modulus for through-thickness direction 1290 MPa Shear modulus for through-thickness/transverse 645 MPa
		
Stress-strain curve for cell A input	Stress-strain curve for cell B input	Stress-strain curve for pouch cell input

kN at 3.5 mm displacement, see Fig. 3 (c).

2.3.4. Three-point bending

The three-point bending test fixtures were different for each of the cells. Cell A was bent between two supporting beams with 48 mm diameter, and the top indenting rod punch had a 10 mm diameter, the distance between two supporting beams was 58 mm. For cell B, the cell was bent between two supporting beams with 16 mm diameter, and top punch had the same size with the supporting beam, the distance between two supporting beams was 48 mm. Cell A had a 2.4 kN peak force at displacement 5.3 mm, Cell B had a 3.65 kN peak force at displacement 7 mm, see Fig. 3 (d). It should be noted that while for transverse loading cases such as rod indentation, hemispherical indentation, and compression between two flat plates, the force drop is due to jellyroll failure. For three-point bending, the first drop of the force is due to buckling of the shell casing; then another drop of force is based on shell casing failure and the last drop is because of jellyroll failure.

For the pouch cell, the top rod indenter and two supporting beams had the same diameter of 16 mm and the distance between two supporting beams was 140 mm. The peak force of 0.35 kN happened at 3 mm displacement. The force drop after the peak was due to a hinge formed in the middle of the cell, but there was no short circuit obtained for this test.

2.3.5. Axial/in-plane compression

Axial compression tests were performed for each cylindrical cell between two flat platens, see Fig. 3 (e). For cell A, the end caps were removed to eliminate the effects of the cap assembly and focus on the jellyroll deformation and potential failure. The cut surface had an unevenness of about 2 mm, which caused a low level of force in that section before the full surface comes into contact with the punch and the force starts to rise. This first 2 mm imperfection was removed when comparing to simulation of this specific test. Cell A had a 9 kN peak force, then the buckling happened for the shell casing which caused the force to dropp to 6 kN before eventually increasing again to 12 kN. Cell B had a 12 kN peak force at 8 mm displacement before buckling and then dropped to 9 kN before increasing to 12 kN at the end of the experiment.

For the in-plane compression test on the pouch cell, a confined set up was used, where the cell is held between rigid flat plates on the large surfaces during in-plane loading. The punch compression applied to the thickness of the cell continues until it has traveled approximately one-third of the cell's vertical length, approximately 33 mm here. No force drop was obtained during the whole procedure for the pouch cell.

3. Computational modeling

The three cells studied here had previously been modeled in the commercial software LS-DYNA for prediction of load-displacement [50,53]. However, the failure prediction in those models involved a recalibration of tensile failure strain value separately for each loading scenario. In the current project, the models were all moved to the commercial software RADIOSS to couple the material model with the implemented /FAIL/SAHRAEI criterion for predicting failure of jellyroll/electrode stack. The purpose was to evaluate whether using a failure locus based on RVE simulations (/FAIL/SAHRAEI) that defines in-plane tensile failure strain as a function of the ratio of through thickness compressive strain over in-plane tensile strain can predict the failure in all loading scenarios with one single model. The HyperCrash software from ALTAIR HyperWorks was used for model conversion from LS-DYNA to RADIOSS. The material model used for the jellyroll/electrode stack was /MAT/HONEYCOMB material model in RADIOSS which is equivalent to MAT_HONEYCOMB which was used in LS-DYNA. The rigid indenter parts in LS-DYNA were converted to elastic parts with a rigid designation in RADIOSS. Those conversions were done automatically. However, after the model was converted using HyperCrash, a series of manual changes were also performed to make the model ready for solution by the RADIOSS solver. These included:

Table 3
Failure strain comparison for honeycomb material for cylindrical cell A [50].

Jellyroll failure definition	Load Condition	Failure Strain
2 plate compression	Dominantly compressive	0.083
Rod indentation	Regions with combined tension and compression	0.33
Hemispherical indentation	Regions with combined tension and compression	0.33
Three-point bending	Separate regions of tension and compression. Lower resistance to tension compared to compression in the direction of bending stresses	0.47

- Converting the engineering stress-strain curves from LS-DYNA to true stress-strain curves for honeycomb material in RADIOSS.
- Removing extra copies of the interface and time history cards.
- For cells with metal casing that were modeled with Hill's material model in LS-DYNA, the Hill_Tab model in RADIOSS needs to be defined manually.
- The Modified Mohr Coulomb (MMC) failure criteria for the shell casing in LS-DYNA needs to be updated to the BIQUAD failure model in RADIOSS.

All material properties and parameters used for the jellyroll is shown in Table 2. For full calibration details of these parameters, interested readers are referred to previous publications of the authors [50,53,70].

In previous iterations, the jellyroll models in LS-DYNA were coupled with maximum tensile strain for failure prediction, where the strain

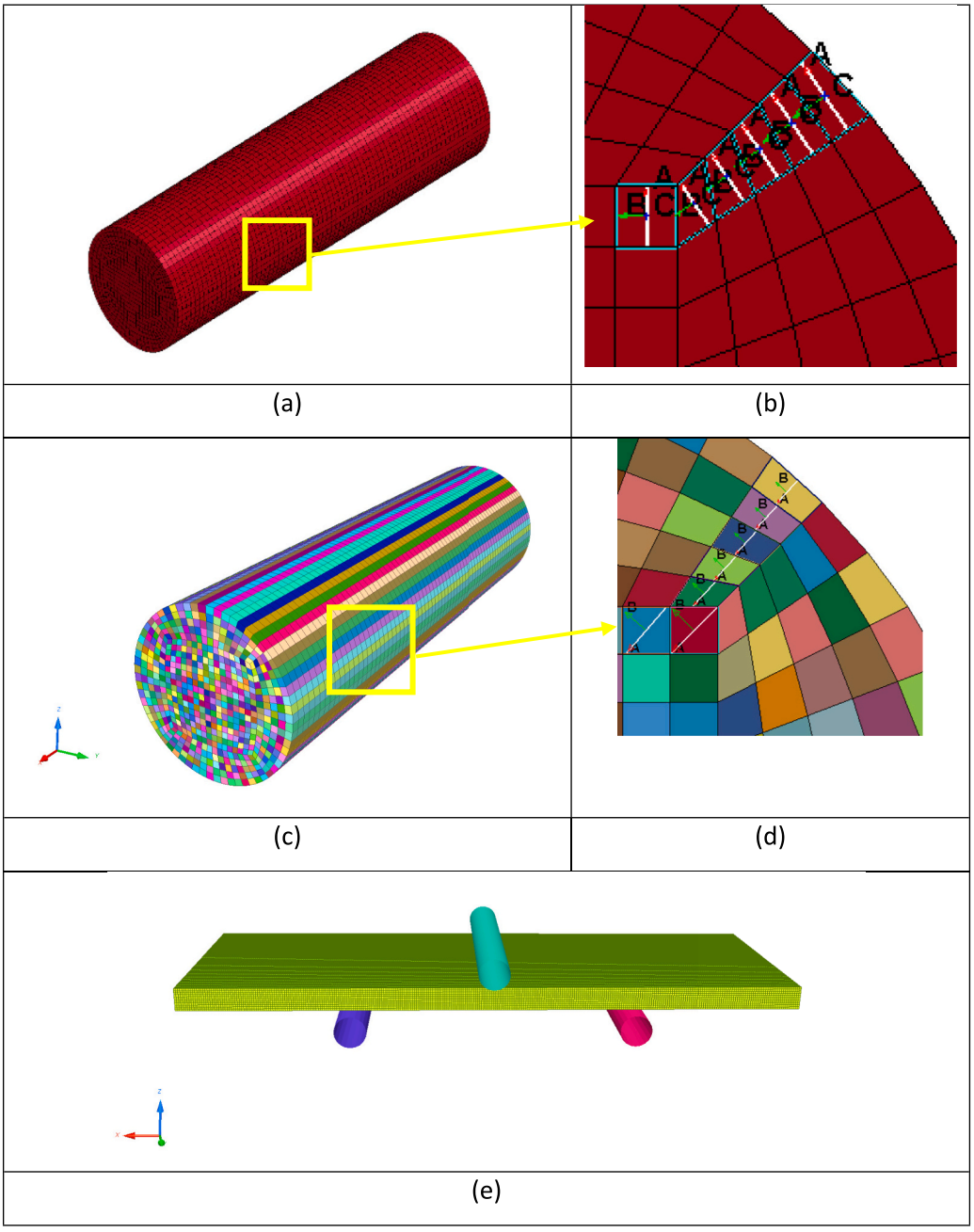


Fig. 4. Finite element model of the jellyroll with element orientation (a) jellyroll before aligned in LS-DYNA (b) elements before aligned. A:tangential; B:radial; C: axial (c) jellyroll after aligned in RADIOSS (d) element after aligned. A: radial; B:tangential; C:axial. (e) pouch cell model under three-point bending set up.

Table 4
R square for all simulations.

Cell A	R Square	Cell B	R Square	Pouch cell	R Square
3pb	0.9759	3pb	0.906	3 PB	0.9625
Flat	0.9791	Flat	0.981063	Flat	0.9973
Hemi	0.9894	Hemi	0.984	S Hemi	0.9946
Rod	0.999	Rod	0.9867	Rod	0.9963
Axial	0.84	Axial	0.8966	M Hemi	0.99452
				In plane	0.9948

values were different between different loading cases, as shown in Table 3. Using the /FAIL/SAHRAEI criterion, programmed in RADIOSS allows the model to use one criterion with the one failure locus as input to be used in all loading scenarios without a need to change any parameters in the input deck. However, it should be noted that in RADIOSS, the honeycomb material uses true stress and true strain. Therefore, the strain values at failure will need to be re-calibrated to generate the full failure locus as the input curve, see Section 4.

Another important point is that the RVE based criterion is using the strains in three directions of anisotropy of the cell, which are aligned with machine direction, transverse direction and through thickness direction of the separator. Therefore, a proper coordinate system for identifying the orientation of battery layers is very important for correct application of this failure model. In the previous models, the solid elements' orientations were defined based on the nodes on each element. With a relatively cylindrical mesh, the elements on the exterior of a cylindrical cell could have minimal deviation from cylindrical coordinate system. However, moving toward the center, their orientation was not strictly following the cylindrical coordinate. As it can be seen in Fig. 4 (b), In the external layers' elements have one radial, tangential, and axial direction, however for center square elements, they get disordered. To fix this issue, a code was written and implemented in the program to re-align all elements to have the same radial, tangential, and axial direction, as seen in Fig. 4 (d). This alignment makes sure the

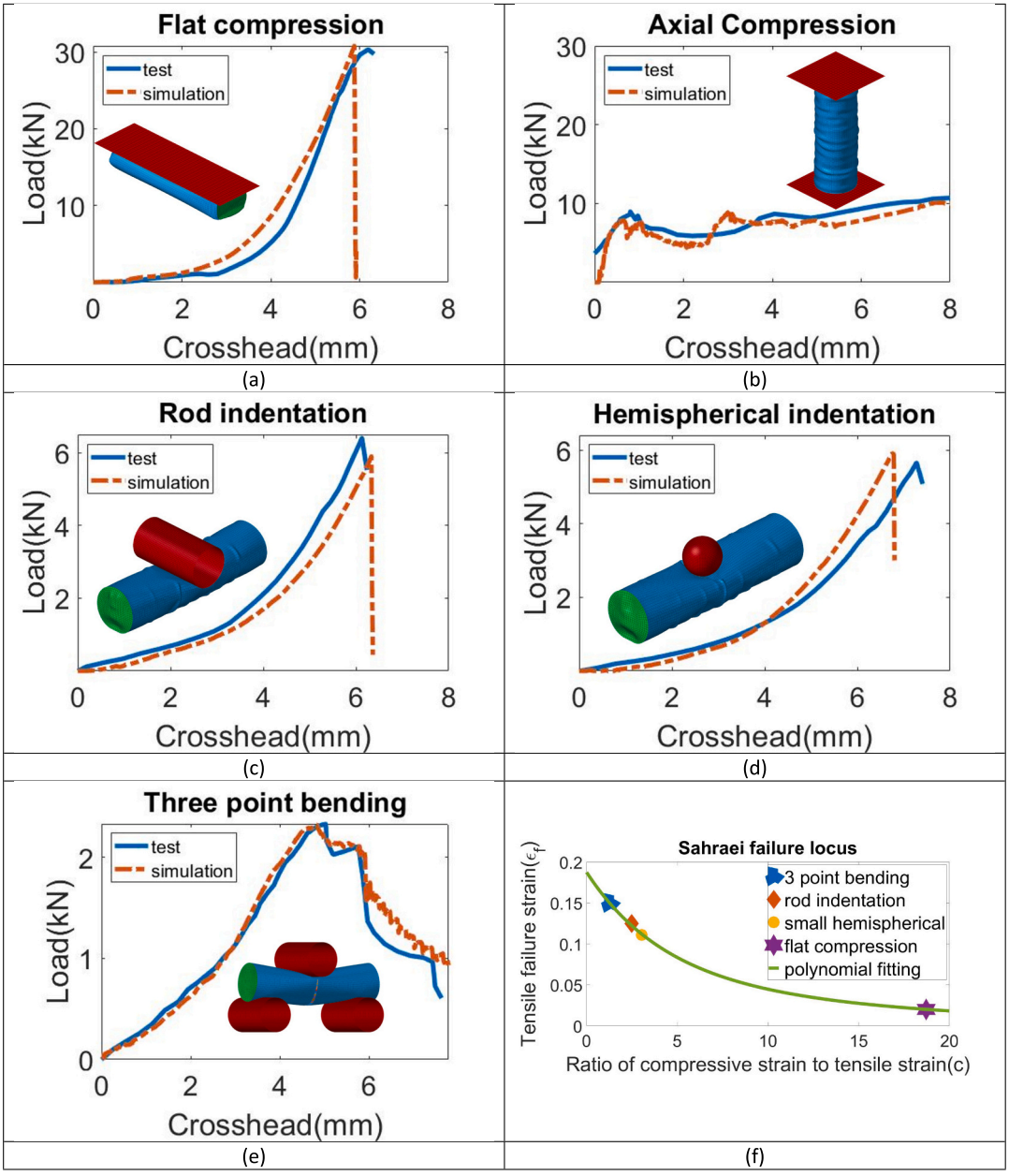


Fig. 5. Simulation result of cell A: (a) Compression between two flat plate (b) Axial compression (c) Rod indentation (d)Hemispherical indentation (e) Three-point bending (f) Failure stain versus ratio of compressive to tensile strain for cell B from RADIOSS.

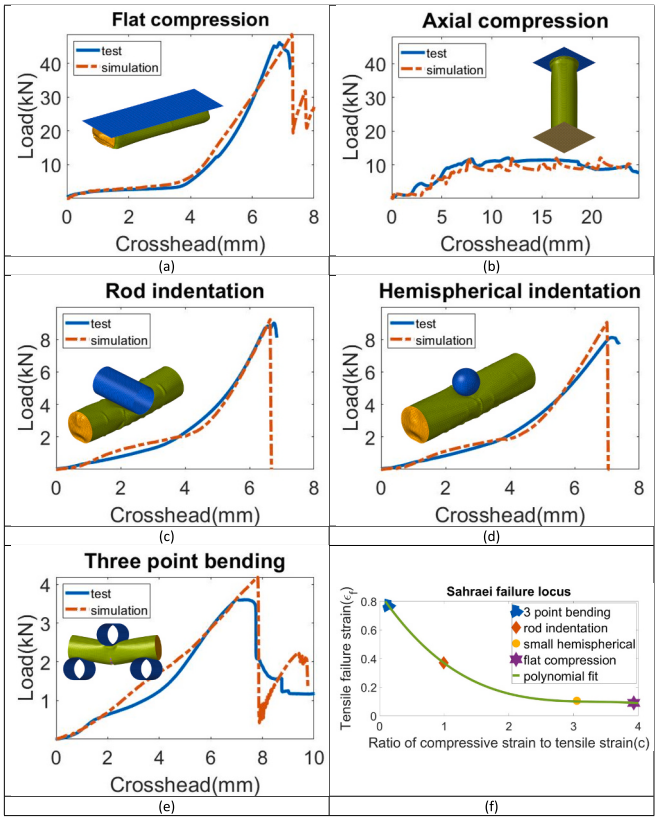


Fig. 6. Simulation result of cell B: (a) Compression between two flat plate (b) Hemispherical indentation (c) Rod indentation (d) Three-point bending (e) Axial compression (f) Failure stain versus ratio of compressive to tensile strain for cell B from RADIOSS.

jellyroll model is getting closer to the reality where the layers are stacked and rolled up to form a cylindrical jellyroll. It should be noted that the axial direction is not shown on Fig. 4 (b) and (d), because the axial direction is pointing perpendicular to the plane of the 2D figures. Such changes in orientations were not needed for the pouch electrode stacks because the layers were oriented in the planes of the elements of the solid elements.

The next section presents the results of the models for all cells simulated using RADIOSS commercial software. Since the jellyroll failure model used was updated to Sahraei failure criterion, no change to the cell model input decks was needed between different loading scenarios. The only changes between different models were the indenter and supporting plates or rods. The average simulation time for each model was about 2.5 h on a local workstation with 20 CPUs.

4. Validation

Here the results of simulations for the cylindrical cells and pouch cell studied are presented and compared to experimental data. For the two 18650 cell models, five loading scenarios were simulated, including global compression between two plates in radial and axial directions, local indentations with hemispherical and rod indenters as well as three-point bending. Both cell models had a good prediction of force-displacement behavior, onset of failure and deformation mode. It should be noted that the universal failure criteria, /FAIL/SAHRAEI, was used and all loading cases had the same input file for the cell model with only changing the punch type and load direction. The pouch cell was simulated under six loading cases, including two different hemispherical indentations, one plane-strain rod indentation, a flat through thickness loading case, an in-plane compression and a three-point bending scenario. The R squares for all simulations versus physical experiments are reported in Table 4.

The through thickness flat compression tests were dominated by global compressive loadings, corresponding to higher compressive to tensile ratios (c_i values), which according Fail Sahraei criterion should result in the smallest failure strains (ϵ_{fi}). For the cylindrical cell A, the jellyroll failed at strain ratio c_3=3.93 with a failure strain of $\epsilon_{f3} = 0.09$, see. For cell B the jellyroll failed at strain ratio c_3=18.92 with a failure strain $\epsilon_{f3} = 0.002$, see Fig. 5 and Fig. 6. For pouch cell, the compressing plate was a round flat plate, still the strain ratio for this load was dominated by global compression, see Fig. 7. The jellyroll failed at strain ratio c_3=4.2 with a failure strain $\epsilon_{f3} = 0.07$.

The axial/in-plane compressions for neither of the cells led to fracture of the jellyroll in the experiments. The simulations predicted the absence of failure for such cases for all three cells. For cell A, the test data was shifted with 2 mm based on the unevenness of surface in the physical test, as mentioned in Section 2. The first peaks in the experimental data of cylindrical cells were due to the buckling of the shell casings, which the models predicted correctly. After the buckling happened, force began to drop, and the jellyroll strength then became the dominating factor. However, as the largest dimension of the cell was in axial direction, the strains in the jellyroll remained small even at the conclusion of the experiments. This prevented an internal short circuit and failure in the jellyroll from developing in such cases. It should be noted that these loading cases can still lead to short circuits in the end cap or tabs of the cell; however, this type of external short circuit was not the topic of the current study.

Hemispherical and rod indentation load cases included more localized deformations, with both tensile and compressive components. Deformations were concentrated under the contact aera between the indenter and the cell. The strain ratios for these cases were higher than the strain ratios of the flat compressions, and the failure strain is correspondingly smaller. For cell A under rod indentation, the jellyroll failed at the strain ratio c_3=0.9913 with a failure strain $\epsilon_{f3} = 0.37$; for hemispherical indentation it failed at strain ratio c_3=3.05 with a failure strain $\epsilon_{f3} = 0.105$. as for cell B, under rod indentation the jellyroll failed at strain ratio c_3=2.483 with a failure strain $\epsilon_{f3} = 0.125$; and it failed at strain ratio c_3=3.04 with a failure strain ϵ_{f3}=0.11 for hemispherical indentation, see Fig. 5 and Fig. 6. For the pouch cell, it had one rod indentation and two different hemispherical indentations. The rod indentation had a strain ratio c_3=0.9306 with a failure strain ϵ_{f3}=0.215; the small/medium hemispherical indentations, both had a strain ratio c_3=0.717/0.653, and both had failure strains ϵ_{f3}=0.2, see Fig. 7. From the cylindrical cell simulation results, rod indentation had more compression strain dominating which has a smaller strain ratio; hemispherical indentation had more tension loading and a higher strain ratio. Similar trends were observed for both cells A and B. For the pouch cell, all rod and hemispherical indentations had very close strain ratio and failure strain values.

The three-point bending case creates areas of both in-plane tension and in-plane compression combined with through thickness compression. The shell casing models of cylindrical cells already capture different behavior under tension and compression by the implemented the Modified Mohr Columb failure criteria [50]. Looking at the bottom part, where the failure of the jellyroll happened, the elements in that part were more controlled by tension. Thus, the strain ratio was much smaller than any other cases and the failure strain was higher. For cell A, jellyroll failed at strain ratio c_3=0.136 with a failure strain $\epsilon_{f3} = 0.77$, see Fig. 3 and Fig. 7; for cell B, jellyroll failed at strain ratio c_3=1.275 with a failure strain $\epsilon_{f3} = 0.15$, see Fig. 3 and Fig. 7. The in-plane and three-point bending for the pouch cell didn't have jellyroll failure. The force drop was due to formation of a hinge under the punch rather than rupture of layers.

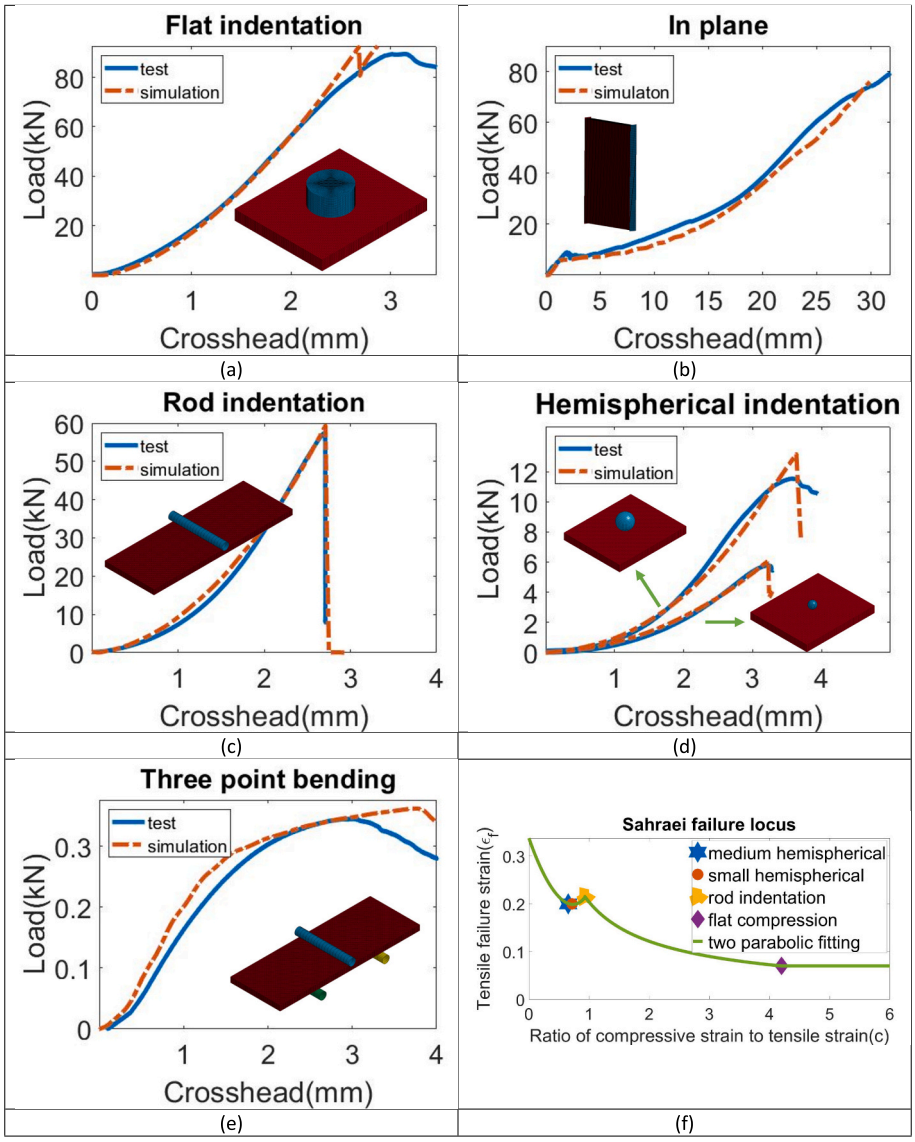


Fig. 7. Simulation result of pouch cell: (a) Flat compression(b) In plane compression test (c) Rod indentation (d) Small/Medium Hemispherical indentation (f) Three-point bending (e) Failure stain versus ratio of compressive to tensile strain for pouch cell from RADIOSS.

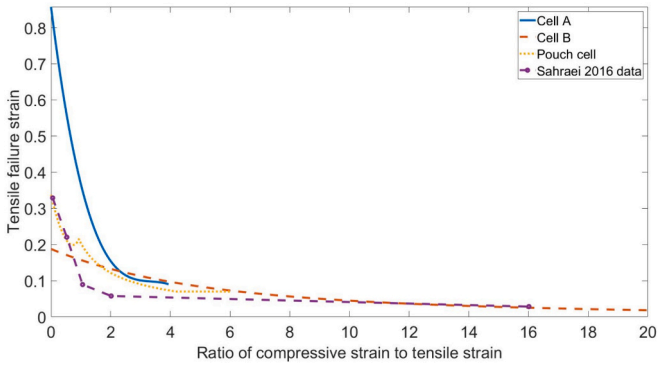


Fig. 8. Failure curve comparison for cell A, cell B and pouch cell.

5. Discussion

We applied Sahraei failure criteria to two cylindrical cells and one pouch cell to predict short circuit under various types of indentation using homogenized models. All simulations show good prediction of the force-displacement behavior and force drop and element erosion at the onset of internal failure. The failure loci of 3 different cell models studied here and the original curve data obtained from RVE model [57] are plotted in Fig. 8. The common trend of these curves is having large failure strain (ϵ_f) value when the strain ratio (c) is low and having small failure strain (ϵ_f) value when strain ratio (c) is high.

Cell A had a significantly higher failure strain (ϵ_f) value compared to all others in low strain ratio region where the three-point bending case falls, and a narrower range of the strain ratios, c between 0 and 4. As this cell is not available anymore for investigation of micro components, it is not clear what the source of such specific properties are. However, it should be noted that this cell was a very early generation of the 18650 cylindrical cells acquired in 2010 and with lithium cobalt chemistry. The range of strain ratios (c) of cell B were from 0 to18, which is also similar to what we found in Sahraei's 2016 work. For the pouch cell, the shape of the failure locus looks like a combination of two parabolic curves. In Fig. 7(f), the hemispherical and rod indentations had very close strain ratios. Considering the size of the pouch cell, these deformations are more localized in the center area and not affecting the whole cell. The similarity of strain rations for different size hemispherical punch loads

explains how earlier literature reported one single value of failure strain could predict all kinds of local hemispherical indentations, see Sahraei's 2012 and 2014 work [7,61].

This failure model also worked for loading cases which didn't have failure. In those cases, like axial compression for cylindrical cells and in-plane compression for pouch cell, elements were compressed and had high values of strain ratio, however the global deformation generated a uniform deformation, thus the strains did not get localized and did not reach the failure criteria. In the cases of the three-point bending loads, the strain ratio (c) was very small, so the cylindrical cells had their largest failure strain (ϵ_f) and the pouch cell did not reach a failure strain at all. It should be noted that the kind of short circuit that the Sahraei failure criterion can predict is the internal short circuit due to the failure of the layers of the jellyroll. There is also another kind of short circuit that is external to the jellyroll and can happen in the endcap assembly, which may happen in axial loading without an internal jellyroll failure.

6. Conclusion

In this study, we calibrated and validated the Sahraei failure criterion for three different cell models: two cylindrical cells and one pouch cell. The theoretical understanding on the sequence of failure in the layers of a jellyroll was developed through RVE simulations, following former research of the team. In the current work, the failure criterion was fully developed and coded in the commercial software Altair RADIOSS, and the failure loci was calibrated for three cells. Then the calibrated failure loci were used to predict onset of internal short circuit in jellyroll or electrode stacks in a variety of load cases. The loadings included flat and axial compressions, rod and hemispherical indentations and three-point bending for cylindrical cells. For pouch cells, the loadings included flat and in-plane compressions, rod and two hemispherical indentations and three-point bending. All cell models coupled with Sahraei failure criterion predicted the force-displacement and onset of short circuit in the jellyrolls and electrode stacks with high accuracy. Future extension of this work will include validations in load-cases with soft support to generate additional strain ratios, as well as considering the effects of SOC, temperature, and strain rate on the failure model.

CRediT authorship contribution statement

Yihan Song: Writing – original draft, Visualization, Validation, Methodology, Formal analysis. **Marian Bulla:** Supervision, Software, Resources, Methodology, Investigation. **Huzefa Patanwala:** Resources, Formal analysis, Data curation. **Elham Sahraei:** Writing – review & editing, Supervision, Resources, Project administration, Funding acquisition, Conceptualization.

Declaration of competing interest

The authors declare that they have no known competing financial interests or personal relationships that could have appeared to influence the work reported in this paper.

Data availability

Data will be made available on request.

Acknowledgement

The authors would like to acknowledge the funding from multiple sources for this research. This includes support of Temple University Startup funds, MIT Industrial battery consortium, and Office of Naval Research Contracts N000141912351 and N000142312612. This research includes calculations carried out on HPC resources supported in part by the National Science Foundation through major research instrumentation grant number 1625061 and by the US Army Research Laboratory under contract number W911NF-16-2-0189.We also like to express sencere thanks to the OpenRadioss team for supporting the implementation of the code and resolving all technical questions throughout the project.

References

[1] Fabiana Meijon Fadul. Estimated global lithium-ion battery demand in electric vehicles (EVs) in 2019 with a forecast for 2020 through 2030, by region.
[2] V. Muenzel, A.F. Hollenkamp, A.I. Bhatt, et al., A comparative testing study of commercial 18650-format lithium-ion battery cells, J. Electrochem. Soc. 162 (8) (2015) A1592–A1600, https://doi.org/10.1149/2.0721508jes.
[3] M. Ouyang, M. Zhang, X. Feng, et al., Internal short circuit detection for battery pack using equivalent parameter and consistency method, J. Power Sources 294 (2015) 272–283, https://doi.org/10.1016/j.jpowsour.2015.06.087.
[4] S. Abada, G. Marlair, A. Lecocq, M. Petit, V. Sauvant-Moynot, F. Huet, Safety focused modeling of lithium-ion batteries: a review, J. Power Sources 306 (2016) 178–192, https://doi.org/10.1016/j.jpowsour.2015.11.100.
[5] Kalnaus S, Wang Y, Turner JA. Mechanical behavior and failure mechanisms of Li-ion battery separators Sergiy Kalnaus *, Yanli Wang, John A. Turner Oak Ridge National Laboratory, Oak Ridge, TN 37831–6164, USA. :1–18.
[6] E. Sahraei, J. Campbell, T. Wierzbicki, Modeling and short circuit detection of 18650 Li-ion cells under mechanical abuse conditions, J. Power Sources 220 (2012) 360–372, https://doi.org/10.1016/j.jpowsour.2012.07.057.
[7] E. Sahraei, R. Hill, T. Wierzbicki, Calibration and finite element simulation of pouch lithium-ion batteries for mechanical integrity, J. Power Sources 201 (2012) 307–321, https://doi.org/10.1016/j.jpowsour.2011.10.094.
[8] G.Z. Voyiadjis, E. Akbari, P.I. Kattan, Damage model for lithium-ion batteries with experiments and simulations, J. Energy Storage 2023 (57) (September 2022) 106285, https://doi.org/10.1016/j.est.2022.106285.
[9] L. Greve, C. Fehrenbach, Mechanical testing and macro-mechanical finite element simulation of the deformation, fracture, and short circuit initiation of cylindrical Lithium ion battery cells, J. Power Sources 214 (2012) 377–385, https://doi.org/10.1016/j.jpowsour.2012.04.055.
[10] S.H. Chung, T. Tancogne-Dejean, J. Zhu, H. Luo, T. Wierzbicki, Failure in lithium-ion batteries under transverse indentation loading, J. Power Sources 2018 (389) (September 2017) 148–159, https://doi.org/10.1016/j.jpowsour.2018.04.003.
[11] M. Bulla, S. Kolling, E. Sahraei, A material model for the orthotropic and viscous behavior of separators in lithium-ion batteries under high mechanical loads, Energies 14 (15) (2021), https://doi.org/10.3390/en14154585.
[12] M.Y. Ali, W.J. Lai, J. Pan, Computational models for simulations of lithium-ion battery cells under constrained compression tests, J. Power Sources 242 (2013) 325–340, https://doi.org/10.1016/j.jpowsour.2013.05.022.
[13] Y. An, H. Jiang, A finite element simulation on transient large deformation and mass diffusion in electrodes for lithium ion batteries, Model Simul. Mater. Sci. Eng. 21 (7) (2013), https://doi.org/10.1088/0965-0393/21/7/074007.
[14] T. Wierzbicki, E. Sahraei, Homogenized mechanical properties for the jellyroll of cylindrical Lithium-ion cells, J. Power Sources 241 (2013) 467–476, https://doi.org/10.1016/j.jpowsour.2013.04.135.
[15] B. Liu, S. Yin, J. Xu, Integrated computation model of lithium-ion battery subject to nail penetration, Appl. Energy 183 (2016) 278–289, https://doi.org/10.1016/j.apenergy.2016.08.101.
[16] Y. Xia, G. Chen, Q. Zhou, X. Shi, F. Shi, Failure behaviours of 100% SOC lithium-ion battery modules under different impact loading conditions, Eng. Fail Anal. 82 (2017) 149–160, https://doi.org/10.1016/j.engfailanal.2017.09.003.
[17] J. Deng, C. Bae, J. Marcicki, A. Masias, T. Miller, Safety modelling and testing of lithium-ion batteries in electrified vehicles, Nat. Energy 3 (4) (2018) 261–266, https://doi.org/10.1038/s41560-018-0122-3.
[18] M.M. Keshavarzi, M. Gilaki, E. Sahraei, Characterization of in-situ material properties of pouch lithium-ion batteries in tension from three-point bending tests, Int. J. Mech. Sci. 219 (2022) 107090, https://doi.org/10.1016/j.ijmecsci.2022.107090.
[19] M. Sheikh, S. Rehman, M. Elkady, Numerical simulation model for short circuit prediction under compression and bending of 18650 cylindrical lithium-ion battery, Energy Procedia 151 (2018) 187–193, https://doi.org/10.1016/j.egypro.2018.09.046.
[20] T. Tancogne-dejean, C.C. Roth, V. Grolleau, T. Beerli, D. Mohr, Using miniature experiments to reveal strength gradients in battery casings, Int. J. Mech. Sci. (2024) 109253, https://doi.org/10.1016/j.ijmecsci.2024.109253. Published online.
[21] X. Zhang, T. Wierzbicki, Characterization of plasticity and fracture of shell casing of lithium-ion cylindrical battery, J. Power Sources 280 (2015) 47–56, https://doi.org/10.1016/j.jpowsour.2015.01.077.
[22] F. Zhu, R. Zhou, D. Sypeck, J. Deng, C. Bae, Failure behavior of prismatic Li-ion battery cells under abuse loading condition - a combined experimental and computational study, J. Energy Storage. 48 (2022) 103969, https://doi.org/10.1016/J.EST.2022.103969.
[23] K.P. Logakannan, F. Zhu, D. Sypeck, S. Xu, J. Deng, S. Kim, Testing and modeling of vehicle Li-ion battery module with prismatic cells under abuse conditions, Energies 16 (3) (2023) 1–17, https://doi.org/10.3390/en16031055.
[24] F. Zhu, Failure behavior of prismatic Li-ion battery cells under abuse loading condition - A combined experimental and computational study, J. Energy Storage 48 (2024) 103969. Published online.

[25] M. Raffler, W. Sinz, S. Erker, B. Brunnsteiner, C. Ellersdorfer, Influence of loading rate and out of plane direction dependence on deformation and electro-mechanical failure behavior of a lithium-ion pouch cell, J. Energy Storage 56 (PA) (2022) 105906, https://doi.org/10.1016/j.est.2022.105906.
[26] D. Qin, P. Wang, T. Wang, J. Chen, Modeling and dynamic impact analysis of prismatic lithium-ion battery, Sustain 15 (10) (2023), https://doi.org/10.3390/su15108414.
[27] M. Bulla, C. Schmandt, S. Kolling, T. Kisters, E. Sahraei, An experimental and numerical study on charged 21700 Lithium-ion battery cells under dynamic and high mechanical loads, Energies 16 (1) (2023), https://doi.org/10.3390/en16010211.
[28] M. Bulla, S. Kolling, E. Sahraei, An experimental and computational study on the orthotropic failure of separators for lithium-ion batteries, Energies 13 (17) (2020), https://doi.org/10.3390/en13174399.
[29] C. Yuan, L. Wang, S. Yin, J. Xu, Generalized separator failure criteria for internal short circuit of lithium-ion battery, J. Power Sources 467 (May) (2020) 228360, https://doi.org/10.1016/j.jpowsour.2020.228360.
[30] S. Kalnaus, Y. Wang, J.A. Turner, Mechanical behavior and failure mechanisms of Li-ion battery separators, J. Power Sources 348 (2017) 255–263, https://doi.org/10.1016/j.jpowsour.2017.03.003.
[31] L. Wang, Y. Jia, J. Xu, Mechanistic understanding of the electrochemo-dependent mechanical behaviors of battery anodes, J. Power Sources 510 (June) (2021) 230428, https://doi.org/10.1016/j.jpowsour.2021.230428.
[32] C. Zhang, J. Xu, L. Cao, Z. Wu, S. Santhanagopalan, Constitutive behavior and progressive mechanical failure of electrodes in lithium-ion batteries, J. Power Sources 357 (2017) 126–137, https://doi.org/10.1016/j.jpowsour.2017.04.103.
[33] Y. Xia, T. Wierzbicki, E. Sahraei, X. Zhang, Damage of cells and battery packs due to ground impact, J. Power Sources 267 (2014) 78–97, https://doi.org/10.1016/j.jpowsour.2014.05.078.
[34] S.R. Shinde, Y. Song, E. Sahraei, Modeling Electric Vehicle's Battery Module using Computational Homogenization Approach 2023, 2023.
[35] M. Serhan, M. Sprowls, D. Jackemeyer, et al., Mechanical properties of commercial copper current- collector foils, Jianyu Zhu,Jiemin Feng, Zhansheng Guo 2012 (2012), https://doi.org/10.1039/x0xx00000x.
[36] Y. Tomioka, N. Yuki, Bend stiffness of copper and copper alloy foils, J. Mater. Process. Technol. 146 (2) (2004) 228–233, https://doi.org/10.1016/j.jmatprotec.2003.11.017.
[37] T. Tancogne-Dejean, D. Mohr, Indentation of small format Lithium-ion pouch cells: experiments and modeling, Int. J. Solids Struct. 257 (June) (2022) 111900, https://doi.org/10.1016/j.ijsolstr.2022.111900.
[38] Y. Wang, Y. Xing, Q.M. Li, A hyper-viscoelastic model for battery separators based on inverse-stress-solution parametrical calibration method, Int. J. Mech. Sci. 225 (May) (2022), https://doi.org/10.1016/j.ijmecsci.2022.107361.
[39] J. Xu, B. Liu, D. Hu, State of charge dependent mechanical integrity behavior of 18650 lithium-ion batteries, Sci. Rep. 6 (February) (2016) 1–11, https://doi.org/10.1038/srep21829.
[40] F. Shi, Z. Song, P.N. Ross, G.A. Somorjai, R.O. Ritchie, K. Komvopoulos, Failure mechanisms of single-crystal silicon electrodes in lithium-ion batteries, Nat. Commun. 7 (July) (2016) 1–8, https://doi.org/10.1038/ncomms11886.
[41] H. Luo, Y. Xia, Q. Zhou, Mechanical damage in a lithium-ion pouch cell under indentation loads, J. Power Sources 357 (2017) 61–70, https://doi.org/10.1016/j.jpowsour.2017.04.101.
[42] X. Zhang, J. Zhu, E. Sahraei, Degradation of battery separators under charge-discharge cycles, RSC Adv. 7 (88) (2017) 56099–56107, https://doi.org/10.1039/c7ra11585g.
[43] H. Luo, J. Zhu, E. Sahraei, Y. Xia, Adhesion strength of the cathode in lithium-ion batteries under combined tension/shear loadings, RSC Adv. 8 (8) (2018) 3996–4005, https://doi.org/10.1039/c7ra12382e.
[44] S. Kalnaus, A. Kumar, Y. Wang, et al., Strain distribution and failure mode of polymer separators for Li-ion batteries under biaxial loading, J. Power Sources 2018 (378) (November 2017) 139–145, https://doi.org/10.1016/j.jpowsour.2017.12.029.
[45] A. Barai, R. Tangirala, K. Uddin, et al., The effect of external compressive loads on the cycle lifetime of lithium-ion pouch cells, J. Energy Storage 13 (2017) 211–219, https://doi.org/10.1016/j.est.2017.07.021.
[46] J. Lian, T. Wierzbicki, J. Zhu, W. Li, Prediction of shear crack formation of lithium-ion batteries under rod indentation: comparison of seven failure criteria, Eng. Fract. Mech. 217 (June) (2019) 106520, https://doi.org/10.1016/j.engfracmech.2019.106520.
[47] E. Orowan, Fracture and strength of solids, Reports Prog. Phys. 12 (1) (1949) 185–232, https://doi.org/10.1088/0034-4885/12/1/309.
[48] T. Wierzbicki, Y. Bao, Y.W. Lee, Y. Bai, Calibration and evaluation of seven fracture models, Int. J. Mech. Sci. 47 (4–5) (2005) 719–743, https://doi.org/10.1016/J.IJMECSCI.2005.03.003.
[49] E. Sahraei, R. Hill, T. Wierzbicki, Calibration and finite element simulation of pouch lithium-ion batteries for mechanical integrity, J. Power Sources 201 (2012) 307–321, https://doi.org/10.1016/j.jpowsour.2011.10.094.
[50] Y. Song, M. Gilaki, M.M. Keshavarzi, E. Sahraei, A universal anisotropic model for a lithium-ion cylindrical cell validated under axial, lateral, and bending loads, Energy Sci. Eng. 10 (4) (2022) 1431–1448, https://doi.org/10.1002/ese3.1111.
[51] G.Z. Voyiadjis, E. Akbari, B. Łuczak, W. Sumelka, Towards determining an engineering stress-strain curve and damage of the cylindrical lithium-ion battery using the cylindrical indentation test, Batteries 9 (4) (2023), https://doi.org/10.3390/batteries9040233.
[52] L. Wang, S. Yin, J. Xu, A detailed computational model for cylindrical lithium-ion batteries under mechanical loading: from cell deformation to short-circuit onset, J. Power Sources 2019 (413) (October 2018) 284–292, https://doi.org/10.1016/j.jpowsour.2018.12.059.
[53] M. Gilaki, Homogenized characterization of cylindrical Li-ion battery cells using elliptical approximation November, 2021, pp. 1–16, https://doi.org/10.1002/er.7531.
[54] E. Sahraei, J. Meier, T. Wierzbicki, Characterizing and modeling mechanical properties and onset of short circuit for three types of lithium-ion pouch cells, J. Power Sources 247 (2014) 503–516, https://doi.org/10.1016/j.jpowsour.2013.08.056.
[55] E. Sahraei, M. Kahn, J. Meier, T. Wierzbicki, Modelling of cracks developed in lithium-ion cells under mechanical loading, RSC Adv. 5 (98) (2015) 80369–80380, https://doi.org/10.1039/c5ra17865g.
[56] C. Zhang, J. Xu, L. Cao, Z. Wu, S. Santhanagopalan, Constitutive behavior and progressive mechanical failure of electrodes in lithium-ion batteries, J. Power Sources 357 (2017) 126–137, https://doi.org/10.1016/j.jpowsour.2017.04.103.
[57] E. Sahraei, E. Bosco, B. Dixon, B. Lai, Microscale failure mechanism[1] E. Sahraei, E. Bosco, B. Dixon, and B. Lai, "Microscale failure mechanisms leading to internal short circuit in Li-ion batteries under complex loading scenarios," J. Power Sources, vol. 319, pp. 56–65, 2016, doi: 10.1016/j, J. Power Sources 319 (2016) 56–65, https://doi.org/10.1016/j.jpowsour.2016.04.005.
[58] No Title. www.openradioss.org.
[59] J. Xu, B. Liu, L. Wang, S. Shang, Dynamic mechanical integrity of cylindrical lithium-ion battery cell upon crushing, Eng. Fail. Anal. 53 (2015) 97–110, https://doi.org/10.1016/j.engfailanal.2015.03.025.
[60] M. Gilaki, E. Sahraei, Effects of temperature on mechanical response of lithium ion batteries to external abusive loads, in: SAE Technical Papers Vol 2019-April, 2019, https://doi.org/10.4271/2019-01-1002.
[61] E. Sahraei, J. Meier, T. Wierzbicki, Characterizing and modeling mechanical properties and onset of short circuit for three types of lithium-ion pouch cells, J. Power Sources 247 (2014) 503–516, https://doi.org/10.1016/j.jpowsour.2013.08.056.
[62] C. Zhang, S. Santhanagopalan, M.A. Sprague, A.A. Pesaran, Coupled mechanical-electrical-thermal modeling for short-circuit prediction in a lithium-ion cell under mechanical abuse, J. Power Sources 290 (2015) 102–113, https://doi.org/10.1016/j.jpowsour.2015.04.162.
[63] V. Kouznetsova, W.A.M. Brekelmans, F.P.T. Baaijens, Approach to micro-macro modeling of heterogeneous materials, Comput. Mech. 27 (1) (2001) 37–48, https://doi.org/10.1007/s004660000212.
[64] P.M. Suquet, Local and Global Aspects in the Mathematical Theory of Plasticity, 1985.
[65] U. Galvanetto, M.H.F. Aliabadi, Multiscale modeling in solid mechanics: computational approaches, in: Multiscale Model Solid Mech Comput Approaches, 2009, pp. 1–334, https://doi.org/10.1142/p604. Published online.
[66] P. Gupta, P. Gudmundson, Modeling of local electrode stresses and pressures in lithium-ion battery packs using three-dimensional homogenization, J. Power Sources 582 (July) (2023) 233514, https://doi.org/10.1016/j.jpowsour.2023.233514.
[67] G. Kermani, M.M. Keshavarzi, E. Sahraei, Deformation of lithium-ion batteries under axial loading: analytical model and representative volume element, Energy Rep. 7 (2021) 2849–2861, https://doi.org/10.1016/j.egyr.2021.05.015.
[68] G. Kermani, B. Dixon, E. Sahraei, Elliptical lithium-ion batteries: transverse and axial loadings under wet/dry conditions, Energy Sci. Eng. 7 (3) (2019) 890–898, https://doi.org/10.1002/ese3.318.
[69] B. Dixon, A. Mason, E. Sahraei, Effects of electrolyte, loading rate and location of indentation on mechanical integrity of li-ion pouch cells, J. Power Sources 396 (June) (2018) 412–420, https://doi.org/10.1016/j.jpowsour.2018.06.042.
[70] H. Patanwala, Mechanical Modeling of Five Types of Commercial EV Pouch Cells, 2022.